

On resonance line profiles predicted by radiation driven disk wind models.

Daniel Proga¹

1

Received _____; accepted _____

¹JILA, University of Colorado, Boulder, CO 80309-0440; proga@colorado.edu

ABSTRACT

We report on resonance line profiles predicted by radiation driven disk wind models which extend radially one order of magnitude farther out than our previous models. Our main result is that the inclusion of a disk wind at larger radii changes qualitatively and quantitatively the line profiles predicted by the models. Our new models predict line absorption that is significantly stronger than those predicted by old models. Some of the previous line profiles exhibit a doubled-humped structure near the line center which is now replaced by a more plausible single, blueshifted minimum. We emphasize that the improvements in the shape as well as the strength of the absorption were achieved without changing the gross properties of the wind. In particular, our new models do not predict a higher mass-loss rate than the previous models. The main changes in the line profiles are due to the fact that the ratio between the rotational velocity and poloidal velocity of the wind decreases downstream. The new line profiles reproduce well the line absorption of the nova-like variable, IX Vel, and promise to reproduce observations of other cataclysmic variables. This success of the radiation driven disk wind model provides an important link between outflows in OB stars and outflows in active galactic nuclei.

Subject headings: accretion, accretion disks – outflows – novae, cataclysmic variables – galaxies: active – galaxies: nuclei – methods: numerical

1. Introduction

It appears that mass accretion onto compact objects through accretion disks is often accompanied by mass outflow from these disks. For example, disk outflows are observed in active galactic nuclei; non-magnetic cataclysmic variables (CVs); and young stellar objects. In the case of CVs, key evidence for outflows comes from P-Cygni profiles of strong UV lines such as C IV λ 1549. However, the evidence for the outflows is not limited just to the strong UV lines (e.g., Long & Knigge 2002 and references therein). Understanding the outflows in CVs is important because they have been the best observed outflows from compact objects and promise to provide us with insights into all disk outflows. Until recently the interpretation of data was limited to fitting observed profiles to synthetic profiles calculated from kinematic models (e.g., Mauche & Raymond 1987; Drew 1987; Shlosman & Vitello 1993; Knigge, Woods & Drew 1995; Long & Knigge 2002).

The most plausible mechanism for driving the CV outflows is radiation pressure on spectral lines. Recently, numerical hydrodynamic models of 2.5-D, time-dependent radiation driven disk winds have been constructed for application to CV disk winds (Pereyra, Kallman & Blondin 1997; Proga, Stone & Drew 1998, hereafter PSD 98; Proga, Stone & Drew 1999, hereafter PSD 99). These initial studies confirm viability of the radiation driving mechanism. However, the same studies reveal some difficulties in obtaining line profiles matching the observed profiles (Proga et al. 2002, Paper 1 hereafter). The latter is likely true even when we allow for the magnetic field effects (Proga 2003).

We focus here on re-examining pure radiation-driven disk wind models for CVs. In particular, we examine the size of the region where the line is formed and show that what is required to improve the model predictions is to capture the entire line formation region by increasing the radial range of the models. In Section 2, we summarize the key elements of our calculations. The results are presented in Section 3. In Section 4, we discuss key

aspects of the synthetic line profiles and make comparisons with recent observations.

2. Method

For this paper, we recalculated dynamical models presented by PSD 99 and calculated a few new models. We refer a reader to PSD 99 for details on wind models and to Paper 1 for details on line-profile calculations. The computations of line profiles are exactly as in Paper 1. We made only two minor modifications to the models: (i) we increased the outer radius of the computational domain, r_o , from 10 to 100 white dwarf radii and (ii) as in PSD 99, we computed models with the radiation force using the intensity of the radiation integrated over all wavelengths, λ , but also using the intensity of the radiation integrated over the UV band only (i.e., $200 \text{ \AA} \leq \lambda \leq 3200 \text{ \AA}$). We call the former I and the latter I_{UV} . We found that the second modification can change the wind solution (e.g., there is no outflow originating from large radii on the disk) but typically this is not much reflected in the predicted line profiles. On the other hand, the first modification does not change the wind solution but has a significant effect on the predicted line profiles.

3. Results of Profile Calculations

Our basic set of line profiles is based on four hydrodynamical models computed on the larger computational domain with the model parameters as in PSD 99’s models A, B, C, and D (see Table 1). We call our models recalculated with the intensity I on the larger grid A1, B1, C1, D1, respectively, while models recalculated with the intensity I_{UV} on the larger grid are labeled A2, B2, C2, D2. To examine the effect of viewing angle on the line profiles, for each disk wind model we compute line profiles for five inclination angles: $i = 5^\circ, 30^\circ, 55^\circ, 70^\circ$, and 85° . Examining effects of inclination angle is important because

of the strong inclination angle dependence observed in CV spectra. Figure 1 shows some of the model line profiles obtained after scaling to unit continuum level.

To illustrate the key differences between profiles from Paper 1 and our profiles, we present results from the B models and the C models. We mention however, that the changes in the line profiles for the A models and the D models are qualitatively similar to the changes for the B models and the C models.

Table 1 summarizes the main input parameters of the hydrodynamical disk wind models including the mass accretion rate, \dot{M}_a , total stellar luminosity relative to the disk luminosity, x , and resultant total system luminosity, $L_{tot} = L_D + L_* = (1 + x)L_D$. Additionally, the table lists, the gross properties of the disk winds including the mass-loss rate, \dot{M}_w , characteristic velocity of the fast stream at $10r_*$, $v_r(10r_*)$ for model A, B, C, and D and their counterparts for the models based on the larger grid, $v_r(100r_*)$, and flow opening angle, ω .

First, we present our results for a wind for which $\dot{M}_a = \pi \times 10^{-8} M_\odot \text{yr}^{-1}$ and the white dwarf (WD) is assumed to be dark $x = 0$ (model B, B1, and B2). We note that the B models have similar properties, except for \dot{M}_w which is lower for B2 than for models B and B1 (see Table 1). The lower \dot{M}_w in model B2 is due to the fact that the radiation force in model B2 is lower than for models B and B1 as it is computed using I_{UV} , which is lower than I . The absence of a wind model A2 is caused by the same effect, at a more extreme level. The A models are for a relatively low luminosity and a reduction of the driving radiation flux resulting from taking into account only the UV photons makes the total radiation force too weak to overcome the gravity and drive a wind.

The five top panels of Figure 1 (Figs. 1a-1e) compare the profiles for model B as a function of i from Paper 1 (thin solid lines) with the profiles predicted by models B1 and B2 (dashed and thick solid lines, respectively). The line profiles from Paper 1 for $i = 55^\circ$

and 70° show two maximum absorptions almost equally shifted from the line center to the blue and red. This effect is due to the fact that the rotation dominates over expansion in shaping the line profile for $r \lesssim 10r_*$. There is little absorption near the line center. The most obvious change in the profiles caused by taking into account the wind at larger radii is the increase of the absorption near the line center. Our detailed analysis of the line-forming region shows that this central absorption is due to the wind originating at $3 \lesssim r \lesssim 10 r_*$ which has optically thick resonance surfaces at $r \lesssim 30 r_*$ to the photons close to the line center. Thus, the ‘third’ component of the absorption due to the wind at large radii changes qualitatively the shape of the total line profile for $i = 55^\circ$ and 70° and resolves the problem of the two maximum absorptions. For $i \lesssim 30^\circ$, the outer wind significantly contributes the line absorption at all wavelengths.

We note that the red and blue edges of the lines do not change when the wind at larger radii is taken into account (compare thick solid lines with dashed and thin solid lines in Fig. 1). This reflects the fact that the old and new wind solutions are very similar within $10 r_*$ and that the old models capture well the acceleration zone of the fastest part of the wind (e.g., PSD 98). Note that the fastest wind is responsible for the position of the blue edge of the absorption at the lowest inclination.

The line profiles based on our new models have a similar dependence on the inclination angle as the line profiles from Paper 1. Namely, the absorption weakens whereas the scattered emission strengthens as inclination angle increases. Additionally, the red edge is at the line center for $i = 5^\circ$ and moves to the red as i increases for $i < 85^\circ$.

The five bottom panels of Figure 1 (Figs. 1f-1j) compare the profiles for model C as a function of i (thin solid lines) with the profiles predicted by models C1 and C2 (dashed and thick solid lines, respectively). Model C is an example of a strong steady state wind where $\dot{M}_a = \pi \times 10^{-8} M_\odot \text{yr}^{-1}$ and WD radiates at the same rate as the disk, $x = 1$. In analogy

with the B models, the C models have similar properties except for \dot{M}_w , which is lower for C2 than for model C and C1 (see Table 1).

The line profiles for model C (fig.1f-1j) are different from those for model B for $i > 30^\circ$. For model B, the line develops a strong, more or less symmetric, double-peaked emission when seen nearly edge-on whereas for model C, the line develops a typical P Cygni profile with blueshifted absorption and redshifted emission. Additionally, the line is significantly broader for model C than for model B. The rotation of the wind does not dominate over expansion in shaping the line. In particular, the shape and strength of the blueshifted absorption is due to expansion. For $i \lesssim 55^\circ$, there is a rotationally broadened redshifted absorption. The redshifted absorption is weaker and narrower than the expansion-dominated blueshifted absorption.

The contribution from the outer wind causes similar changes to the line profiles for model C as it does to the profiles for model B. The line profiles for model C from Paper 1 show a deep narrow absorption at $v \sim -1000 \text{ km s}^{-1}$ for $i = 70^\circ$ (Fig. 1i) and at $v \sim -200 \text{ km s}^{-1}$ for $i = 85^\circ$ (Fig. 1j). The central absorption due to the outer wind broadens and strengthens the absorption for $i = 70^\circ$ and eliminates the central emission which has a peak at $v \sim -500 \text{ km s}^{-1}$ in the line profile from Paper 1. Additionally, the outer wind strengthens the red-shifted emission for $v \lesssim 1500 \text{ km s}^{-1}$. As a result, for $i = 70^\circ$, the line profiles predicted by models C1 and C2 does not exhibit the double-humped structure seen in the line profile predicted by model C. For $i = 85^\circ$, the line profiles predicted by models C1 and C2 develop a double-peaked emission without the deep narrow absorption at $v \sim -1000 \text{ km s}^{-1}$ which is present in the profile from Paper 1. This narrow absorption disappeared in the profiles for model C1 and C2, mainly because the blue-shifted absorption is weaker in our new model than in the old model.

For $i < 70^\circ$, the line profiles for model B and C are similar in three respects: (i) the

scattered emission is weak, (ii) the contribution from the outer wind is negligible in the red part but it is significant in the blue part of the profiles, and (iii) the contribution from the outer wind does not change the position of the red and blue edges of the lines.

In analogy to models B and C, at $i = 85^\circ$, the scattered emission is seen as weaker by the observer for models C1 and C2 than for models B1 and B2 because the background continuum emission is stronger in the C models. At this high inclination, the background continuum of the C model is dominated by the WD contribution (see Table 1 in Paper 1).

4. Discussion and comparison with observations

Our main result is that the inclusion of a disk wind at larger radii changes qualitatively and quantitatively the line profiles predicted by the pure radiation-driven disk wind model. The models computed on a small grid – such as those in PSD 99, where the outer radius equals $10 r_*$ – are sufficient to calculate the gross properties of the disk wind. For example, PSD 99’s simulations are sufficient to calculate the wind mass-loss rate and the fast part of the wind, which are both associated with the outflow from the innermost disk. However, the previous simulations do not capture the entire region where lines are formed. As a result, they underpredict the line absorption and to a lesser extent the scattered emission. The previous simulations predicted a double-humped structure near the line center for intermediate inclinations. This structure is due to a nonnegligible red-shifted absorption that is formed in the slow wind where the rotational velocity dominates over expansion velocity. We showed here that by taking into account the downstream part of the same slow wind we were able to increase significantly the central absorption. As a result, the double-humped structure is reshaped to a more typical broad trough. We emphasize that all improvements in the shape as well as the strength of the absorption were achieved without changing the gross properties of the wind. In particular, our new models do not

predict a higher mass-loss rate than the previous models. The changes in the line profiles are mainly caused by the fact that the ratio between the rotational and poloidal velocity decreases downstream.

In Paper 1, we showed that the double minimum apparent near line center can be replaced by a more plausible single, blueshifted minimum when we make the slow wind transparent. We concluded then, that the wind-formed line profiles seen at ultraviolet wavelengths cannot originate in a flow where rotation and poloidal expansion are comparable. The UV lines must trace gas that expands substantially faster than it rotates. Our new results support this reasoning.

Our new and old line profiles have many features that are qualitatively consistent with the features of the observed line profiles. These include the classical P-Cygni shape for a range of inclinations, the location of the maximum depth of the absorption component at velocities less than the terminal velocity (a requirement discussed in Drew 1987), and the transition from net absorption to net emission with increasing inclination. However, our new line profiles are also qualitatively consistent with the observations, in particular, the depth and width of the absorption. The main discrepancy between the predicted line profiles and the observed ones is in the line emission. Specifically, the model cannot produce the redshifted emission as strong as that seen, for example, in the CIV profile of many systems with intermediate inclinations (see below). However, this shortcoming is not a great surprise – this has been a problem for a while (see e.g. Mauche, Lee & Kallman 1997; Ko et al. 1998).

We are undertaking a systematic comparison between predicted line profiles and observations for many systems. Such a study is needed to support our finding that the pure radiation-driven disk wind model can work for CV winds in the sense that it can reproduce the observed line profiles for model parameters (e.g., system luminosities) suitable to CVs.

Our preliminary results from limited survey of dynamical models and their predictions are promising. To illustrate this, we compare our new profiles with spectrally well-resolved UV observations for the brightest nova-like variable, IX Vel (Hartley [2002]; in Paper 1, we made a model comparison with the same data). In Figure 2, we show a comparison between profiles derived from the model with $\dot{M}_a = \pi \times 10^{-8} M_\odot \text{yr}^{-1}$, $x = 0.25$ (model E2) and observations of the CIV 1549Å and SiIV 1403Å transitions. To show how much line emission is required we plot only the absorption component of the line synthesized for $i = 50^\circ$ and 60° . The observed i for this system is 60° (Beuermann & Thomas 1990). The choice for the relative luminosity of WD (i.e., $x = 0.25$) was motivated by the fact that the line profiles predicted by model B2 with $x = 0$ and model C2 with $x = 1$ bracket the observed profiles.

Figure 2 clearly shows that the model profiles well reproduce the blue-shifted absorption. Therefore, we conclude that we have significantly narrowed the gap between the kinematics of the radiation-driven models and reality. The gap is only narrowed but not bridged yet because the mass fluxes required to match the observed spectra at least of IX Vel are somewhat higher than those observed. In particular, it is believed that the luminosity of the system requires a mass accretion rate of at most $10^{-8} M_\odot \text{yr}^{-1}$, whereas our line profiles require $\dot{M}_a = \pi \times 10^{-8} M_\odot \text{yr}^{-1}$ and $x = 0.25$, yielding a system luminosity higher than the observed one by a factor of ~ 4 . However, our main point is that this discrepancy is much smaller than it used to be (i.e., it was more than 1 order of magnitude) and we believe that it can be reduced still further. We have computed many models, changing various model parameters such as \dot{M}_a and the parameters of the force multiplier, α and M_{max} . In general, we find that there is a degeneracy in the model parameters as far as line profiles are concerned (PSD 98 found an analogous degeneracy for the wind properties). For example, models with slightly different parameters – such as \dot{M}_a and α – produce similar line profiles for different i . Additionally, a model with the same parameters as model A2 but with $\alpha = 0.674$ instead $\alpha = 0.6$ predicts very similar line profiles to model

B2 for the same i . Finally, we find that the product $(1 + x)L_D M_{max}$, not its individual factors, appears to be a fundamental parameter determining the line profiles (i.e., their width and depth) for the parameter range applicable to CVs. This has an important implication for our models: to obtain a theoretical fit as good as shown in Fig. 2 for a fixed i , we need $(1 + x)L_D M_{max} \sim 1.3 \times 10^5 L_\odot$ rather than specifically $x = 0.25$, $M_{max} = 4400$, and $L_D = 23.4 L_\odot$ as for model E2.

As in Paper 1, some aspects of our results depend on our assumptions about the disk and microphysics of the wind. Further work should include in particular, self-consistent calculations of the wind ionization state.

ACKNOWLEDGMENTS: We thank J.E. Drew and M.C. Begelman for their comments. We acknowledge support from NASA under LTSA grants NAG5-11736 and NAG5-12867. We also acknowledge support provided by NASA through grant AR-09532 from the Space Telescope Science Institute, which is operated by the Association of Universities for Research in Astronomy, Inc., under NASA contract NAS5-26555.

REFERENCES

- Beuermann, K., Thomas, H.-C., 1990, A&A, 230, 326
- Drew, J.E. 1987, MNRAS, 224, 595
- Hartley, L. E., Drew, J. E., Long, K. S., Knigge, C., & Proga, D. 2002, MNRAS, 332, 127
- Knigge, C., Woods, J.A., Drew, J.E. 1995, MNRAS, 273, 225
- Ko, Y., Lee, P. Y., Schlegel, E. M., & Kallman, T. R. 1996, ApJ, 457, 363
- Long, K.S., & Knigge, C., 2002, ApJ, 579, 725
- Mauche, C.W., Lee, Y.P., Kallman, T.R. 1997, ApJ, 477, 832
- Mauche C.W., Raymond J.C. 1987, ApJ, 323, 690
- Mauche C.W., & Raymond J.C. 2000, ApJ, 323, 690
- Pereyra, N.A., Kallman, T.R., & Blondin, J.M. 1997, ApJ, 477, 368
- Proga, D. 2003, ApJ, 585, 406
- Proga, D., Kallman, T.R., Drew, J.E., & Hartley, L.E., 2002, ApJ, 572, 382 (Paper 1)
- Proga, D., Stone J.M., & Drew J.E. 1998, MNRAS, 295, 595 (PSD 98)
- Proga, D., Stone J.M., & Drew J.E. 1999, MNRAS, 310, 476 (PSD 99)
- Shlosman I., & Vitello P.A.J. 1993, ApJ, 409, 372

Figure Captions

Figure 1 – Line profiles for hydrodynamical disk wind models as a function of inclination angle, i (see top right corner of each panel for the value of i). The top panels, a-e, are for models with $x = 0$ but with $\dot{M}_a = \pi \times 10^{-8} M_{\odot} \text{yr}^{-1}$ (B models). The bottom panels, f-j, show results for models with $\dot{M}_a = \pi \times 10^{-8} M_{\odot} \text{yr}^{-1}$ and $x = 1$ (C models). The thin solid lines are the line profiles based on the models B and C from PSD 99 (these are the same profiles as in Paper 1, see figure 1 there). The dashed lines are line profiles based on our models B1 and C1 while the thick solid lines are profiles based on models B2 and C2. The zero velocity corresponding to the line center is indicated by the vertical line. Note the difference in the velocity and flux ranges in the planes for $i = 85^{\circ}$ (fifth column).

Figure 2 – Comparison between profiles derived from model E2 for $i = 50^{\circ}$ and 60° (thick solid and thick dashed line, respectively) and observations of the CIV 1549Å and SiIV 1403Å transitions in the spectrum of the brightest nova-like variable, IX Vel (Hartley et al. [2002]). The synthesized lines show the absorption component without the contribution from the scattered emission (see the main text).

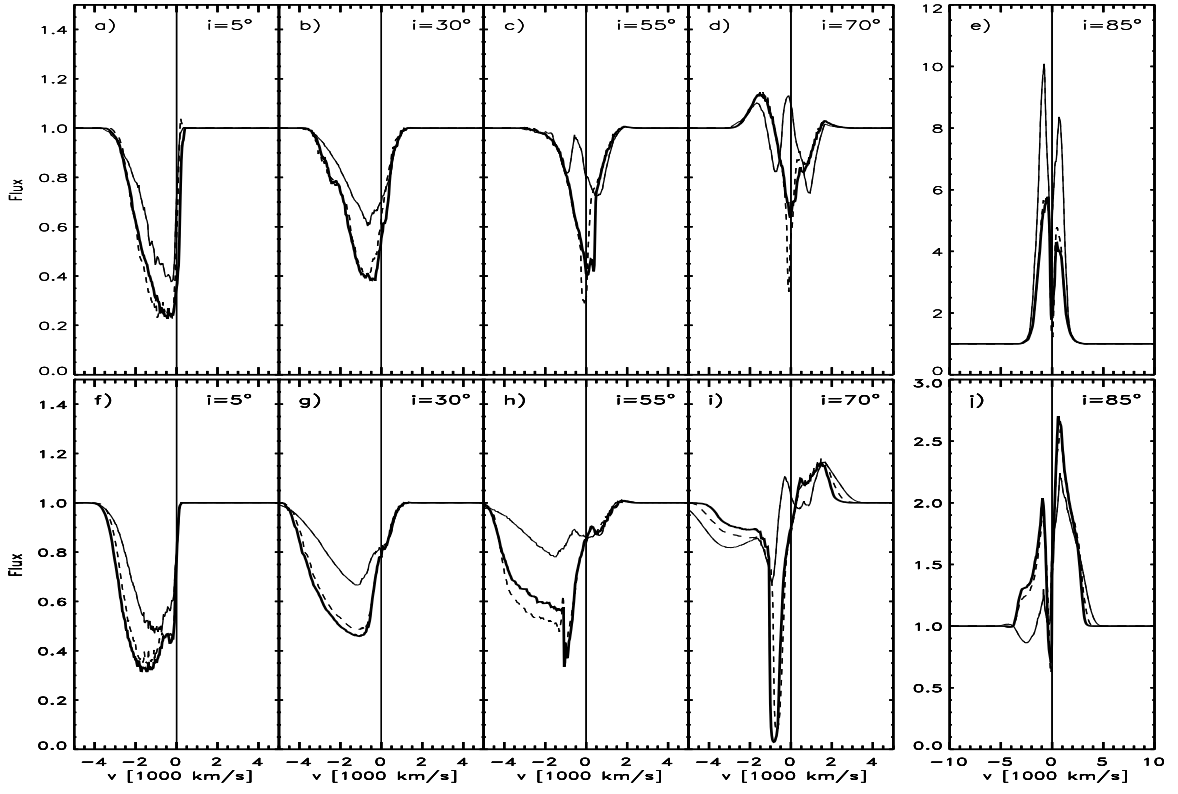


Fig. 1.—

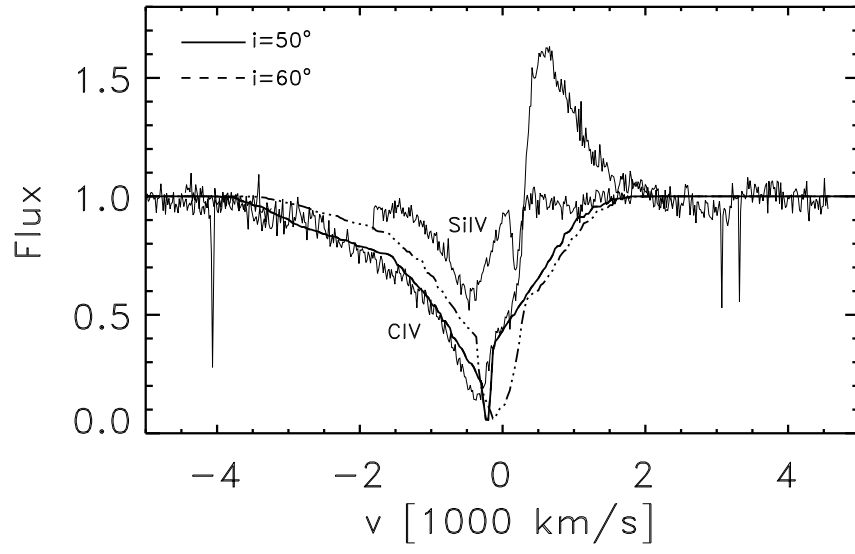


Fig. 2.—

Table 1: Input parameters and main characteristics of the hydrodynamical models used in this paper (for models A, B, C, and D see also PSD 99)

model	\dot{M}_a ($M_\odot \text{ yr}^{-1}$)	x	L_{tot} L_\odot	\dot{M}_w ($M_\odot \text{ yr}^{-1}$)	$v_r(10r_*)$ (km s^{-1})	$v_r(100r_*)$ (km s^{-1})	ω degrees
A	10^{-8}	0	7.5	5.5×10^{-14}	900	–	50
B	$\pi \times 10^{-8}$	0	23.4	4.0×10^{-12}	3500	–	60
C	$\pi \times 10^{-8}$	1	46.9	2.1×10^{-11}	3500	–	32
D	$\pi \times 10^{-8}$	3	93.8	7.1×10^{-11}	5000	–	16
A1	10^{-8}	0	7.5	5.5×10^{-14}	900	900	55
B1	$\pi \times 10^{-8}$	0	23.4	4.0×10^{-12}	3500	3500	65
C1	$\pi \times 10^{-8}$	1	46.9	2.1×10^{-11}	3500	3500	45
D1	$\pi \times 10^{-8}$	3	93.8	7.1×10^{-11}	5000	5000	22
A2	10^{-8}	0	7.5	–	800	–	–
B2	$\pi \times 10^{-8}$	0	23.4	2.2×10^{-12}	3500	3500	65
C2	$\pi \times 10^{-8}$	1	46.9	1.9×10^{-11}	3500	3500	45
D2	$\pi \times 10^{-8}$	3	93.8	6.3×10^{-11}	5000	5000	30
E2	$\pi \times 10^{-8}$	0.25	29.3	8×10^{-12}	3500	3500	55